

# Euclid: Forecast constraints on the cosmic distance duality relation with complementary external probes<sup>★</sup>

M. Martinelli<sup>1,★</sup>, C.J.A.P. Martins<sup>2,3</sup>, S. Nesseris<sup>1</sup>, D. Sapone<sup>4</sup>, I. Tutusaus<sup>5,6</sup>, A. Avgoustidis<sup>7</sup>, S. Camera<sup>8,9,10</sup>, C. Carbone<sup>11</sup>, S. Casas<sup>12</sup>, S. Ilic<sup>13,14,15</sup>, Z. Sakr<sup>15,16</sup>, V. Yankelevich<sup>17</sup>, N. Auricchio<sup>18</sup>, A. Balestra<sup>19</sup>, C. Bodendorf<sup>20</sup>, D. Bonino<sup>10</sup>, E. Branchini<sup>21,22,23</sup>, M. Brescia<sup>24</sup>, J. Brinchmann<sup>3</sup>, V. Capobianco<sup>10</sup>, J. Carretero<sup>25</sup>, M. Castellano<sup>23</sup>, S. Cavioti<sup>24,26,27</sup>, R. Cledassou<sup>28</sup>, G. Congedo<sup>29</sup>, L. Conversi<sup>30,31</sup>, L. Corcione<sup>10</sup>, F. Dubath<sup>32</sup>, A. Ealet<sup>33</sup>, M. Frailis<sup>34</sup>, E. Franceschi<sup>18</sup>, M. Fumana<sup>11</sup>, B. Garilli<sup>11</sup>, B. Gillis<sup>29</sup>, C. Giocoli<sup>35,36,37</sup>, F. Grupp<sup>20,38</sup>, S.V.H. Haugan<sup>39</sup>, W. Holmes<sup>40</sup>, F. Hormuth<sup>41</sup>, K. Jahnke<sup>42</sup>, S. Kermiche<sup>43</sup>, M. Kilbinger<sup>12</sup>, T.D. Kitching<sup>44</sup>, B. Kubik<sup>45</sup>, M. Kunz<sup>46</sup>, H. Kurki-Suonio<sup>47</sup>, S. Ligi<sup>10</sup>, P.B. Lilje<sup>39</sup>, I. Lloro<sup>48</sup>, O. Marggraf<sup>49</sup>, K. Markovic<sup>40</sup>, R. Massey<sup>50</sup>, S. Mei<sup>51</sup>, M. Meneghetti<sup>35,37</sup>, G. Meylan<sup>52</sup>, L. Moscardini<sup>18,36,53</sup>, S. Niemi<sup>44</sup>, C. Padilla<sup>54</sup>, S. Paltani<sup>32</sup>, F. Pasian<sup>34</sup>, V. Pettorino<sup>12</sup>, S. Pires<sup>12</sup>, G. Polenta<sup>55</sup>, M. Poncet<sup>28</sup>, L. Popa<sup>56</sup>, L. Pozzetti<sup>18</sup>, F. Raison<sup>20</sup>, J. Rhodes<sup>40</sup>, M. Roncarelli<sup>18,36</sup>, R. Saglia<sup>20,38</sup>, P. Schneider<sup>49</sup>, A. Secroun<sup>43</sup>, S. Serrano<sup>5,6</sup>, C. Sirignano<sup>57,58</sup>, G. Sirri<sup>53</sup>, F. Sureau<sup>12</sup>, A.N. Taylor<sup>29</sup>, I. Tereno<sup>59,60</sup>, R. Toledo-Moreo<sup>61</sup>, L. Valenziano<sup>18,53</sup>, T. Vassallo<sup>38</sup>, Y. Wang<sup>62</sup>, N. Welikala<sup>29</sup>, J. Weller<sup>20,38</sup>, A. Zacchei<sup>34</sup>

(Affiliations can be found after the references)

29 July 2020

## ABSTRACT

In metric theories of gravity with photon number conservation, the luminosity and angular diameter distances are related via the Etherington relation, also known as the distance-duality relation (DDR). A violation of this relation would rule out the standard cosmological paradigm and point at the presence of new physics. We quantify the ability of *Euclid*, in combination with contemporary surveys, to improve the current constraints on deviations from the DDR in the redshift range  $0 < z < 1.6$ . We start by an analysis of the latest available data, improving previously reported constraints by a factor of 2.5. We then present a detailed analysis of simulated *Euclid* and external data products, using both standard parametric methods (relying on phenomenological descriptions of possible DDR violations) and a machine learning reconstruction using Genetic Algorithms. We find that for parametric methods *Euclid* can (in combination with external probes) improve current constraints by approximately a factor of six, while for non-parametric methods *Euclid* can improve current constraints by a factor of three. Our results highlight the importance of surveys like *Euclid* in accurately testing the pillars of the current cosmological paradigm and constraining physics beyond the standard cosmological model.

**Key words.** Cosmology: observations – (Cosmology:) cosmological parameters – Space vehicles: instruments – Surveys – Methods: statistical – Methods: data analysis

## 1. Introduction

Standard cosmological analyses rely on several explicit or implicit assumptions. Three examples of commonly made assumptions are that the Copernican principle holds (i.e. we are not at a special place in the Universe), that the photon number is conserved, and that the Universe is homogeneous and isotropic, at least on sufficiently large scales. While they are, in some sense, the pillars on which standard cosmology is built and none of them are seriously challenged by current data (for a possible exception see Webb et al. 2011), they are violated in many extensions of the standard cosmological model and of the standard particle physics paradigm, with extensions of the latter being collectively known as beyond the standard model (BSM) theories. Relaxing such assumptions has an observable impact on the so-called Distance Duality Relation (DDR), which is crucial for tests of the background expansion rate of the Universe, as it allows us to relate the luminosity and angular diameter distances,

while at the same time affecting the prediction for the change in redshift of the Cosmic Microwave Background (CMB) radiation temperature. Testing these predictions with cosmological data therefore has the potential to rule out large classes of extended theories or to observe signatures of non-standard physics.

Combining supernova data from the SCP Union 2008 Compilation (Kowalski et al. 2008) and  $H(z)$  data from Stern et al. (2010), the deviation from the standard relation between luminosity and angular diameter distances has been constrained to few percent (Avgoustidis et al. 2010; Ma & Corasaniti 2018). At the same time, direct measurements of CMB temperature at different redshifts, denoted  $T(z)$  hereafter, have been obtained at both low redshifts ( $z \lesssim 1$ ) via observations of the Sunyaev–Zel’dovich effect in galaxy clusters (Luzzi et al. 2009), and at higher redshifts ( $z > 1$ ) through high-resolution spectroscopy of atomic, ionic or molecular levels excited by the absorption of CMB photons (Noterdaeme et al. 2011). The deviation from the standard redshift evolution of CMB temperature has also been constrained to a few percent (Noterdaeme et al. 2011). The combination of distance and temperature measurements as two inde-

<sup>★</sup> This paper is published on behalf of the Euclid Consortium.

<sup>★★</sup> e-mail: matteo.martinelli@uam.es

pendent probes of the same underlying mechanism shrunk the constraints on the deviation of  $T(z)$  to 0.8% (Avgoustidis et al. 2016). Other possible observables to constrain possible violations of the DDR include Galaxy Clusters (Holanda et al. 2010), Sunyaev-Zeldovich effect (Holanda et al. 2012), strong gravitational lensing (Liao et al. 2016), and standard sirens from gravitational waves observations (Liao 2019; Hogg et al. 2020).

Upcoming and more sensitive cosmological surveys for supernovae and Baryon Acoustic Oscillations (BAO) will further tighten the constraints achievable through distance measurements. Here we focus on *Euclid*, an M-class space mission of the European Space Agency due for launch in 2022. It will carry two different instruments onboard: a visible imager (Cropper et al. 2018) and a near-infrared spectrophotometric instrument (Costille et al. 2018). Together they will carry out a photometric and spectroscopic galaxy survey over 15 000 deg<sup>2</sup> of extra-galactic sky with the aim to measure the geometry of the Universe and the growth of structures up to  $z \sim 2$  and beyond (Laureijs et al. 2011).

*Euclid* will have three main cosmological probes: weak lensing and galaxy clustering from the photometric survey, and galaxy clustering from the spectroscopic survey. While photometric galaxy surveys allow for observations of large amounts of galaxies with relatively large redshift uncertainties, spectroscopic galaxy surveys provide information for fewer objects but with much higher radial precision. The spectroscopic accuracy of *Euclid* will allow for precise galaxy clustering analyses including the radial dimension. Here we simulate BAO data from *Euclid* using the Fisher matrix technique, and specifically following the same strategy used in Euclid Collaboration: Blanchard et al. (2019), hereafter EC19, for the spectroscopic survey.

On the other hand, improved direct measurements of the CMB temperature at different redshifts will be available, such as those expected in the coming years from ESPRESSO (Pepe et al. 2013; Leite et al. 2016), and ultimately ELT-HIRES (Liske et al. 2014), and these will significantly improve the available constraining power (Avgoustidis et al. 2014). In addition to this, future observations of gravitational wave events will allow us to exploit standard sirens to obtain luminosity distance measurements at even higher redshifts, thus extending the redshift range of DDR tests (see e.g. Yang et al. 2019).

Our work also highlights some of the synergies between different surveys. Specifically, we will show how data from the Dark Energy Spectroscopic Instrument (DESI, DESI Collaboration: Aghamousa et al. 2016), a survey that aims at probing the expansion rate and large-scale structure (LSS) of the universe, and from the Legacy Survey of Space and Time (LSST), performed by the Vera C. Rubin Observatory (LSST Science Collaboration: Abell et al. 2009) can complement the *Euclid* BAO survey and extend the probed redshift range.

In Amendola et al. (2018) forecast constraints on deviations from the standard DDR were presented, combining a dark energy task force stage IV supernova mission (Albrecht et al. 2006, taking SNAP as a concrete example) and the galaxy survey expected to be performed by the *Euclid* satellite (Laureijs et al. 2011). In this paper we aim to update and extend these results; specifically, we rely on more recent *Euclid* specifications (see EC19) and we investigate possible synergies between this survey and contemporary observations. We also refine the analysis done in Amendola et al. (2018); we follow the common approach of encoding DDR violations in the phenomenological function  $\epsilon(z)$ , but, alongside the common constant parameterization, we include here a binning in redshift of this function in order to understand if current or future data are able to detect a redshift trend.

Moreover, we also apply a more refined machine learning technique to reconstruct  $\epsilon(z)$  with a minimal set of assumptions, performing our analysis with the use of Genetic Algorithms (Bogdanos & Nesseris 2009; Nesseris & Garcia-Bellido 2012).

After reviewing the theoretical background of the DDR in Sect. 2, we describe the different analyses done in this work to test the relation in Sect. 3, detailing both our parameterized approach and the agnostic reconstruction. We then present the constraints obtained from current observations in Sect. 4. The results of this analysis are used as a fiducial cosmology for the mock data we produce in Sect. 5, and then compared with forecast results, which are discussed in Sect. 6. Finally, we draw our conclusions in Sect. 7.

## 2. Extensions of the Distance Duality Relation

In any cosmological model based on a metric theory of gravity, the Etherington relation (Etherington 1933), also known as the DDR, implies that distance measures are unique. The luminosity distance,  $d_L(z)$ , is related to the angular diameter distance,  $d_A(z)$ , as

$$d_L(z) = (1+z)^2 d_A(z), \quad (1)$$

with the angular diameter distance obtained in terms of the Hubble parameter  $H(z)$  as

$$d_A(z) = \frac{c}{1+z} \int_0^z \frac{dz'}{H(z')}. \quad (2)$$

This relation is valid in any cosmological background where photons travel on null geodesics and where, crucially, the photon number is conserved, within the assumption of a flat Universe with a negligible curvature contribution to the total energy density ( $\Omega_{k,0} = 0$ ).

On the other hand, if the expansion of the Universe is adiabatic and the CMB spectrum was a black-body at the time it originated, such a property will be preserved by the subsequent cosmological evolution, with the CMB temperature evolving as

$$T(z) = T_0(1+z). \quad (3)$$

This is a robust prediction of standard cosmology, but it is violated in many non-standard models, including scenarios involving photon mixing (for a review see Jaeckel & Ringwald 2010) and the violation of photon number conservation. Throughout this paper we assume that the cosmological principle holds, i.e. that the Universe is, to first approximation, homogeneous and isotropic. Consequently, we do not investigate any possible dependence of the DDR on the direction of the sky, and only tackle its possible redshift dependence (for further discussion on the validity of such assumption see e.g. Maartens 2011; Ntelis et al. 2017).

In extended theories, where this latter property does not hold, we expect deviations from both Eq. (1) and Eq. (3); therefore an analysis of such behaviour could in principle benefit from the complementarity between galaxy and supernova surveys, probing departures from the DDR, and spectroscopic tests of  $T(z)$  evolution, both of which will be available during the next decade.

Deviations from the Etherington relation are commonly parameterized as

$$d_L(z) = (1+z)^{2+\epsilon(z)} d_A(z), \quad (4)$$

where the function  $\epsilon(z)$  is usually assumed to be constant and, using currently available data, its value is constrained to be  $O(10^{-2})$

(Avgoustidis et al. 2009, 2010). As the precision of the data improves, and the available redshift range is extended, the DDR could be probed at larger redshifts,  $z \gtrsim 2$ , and tighter constraints of a possible redshift dependence could, in principle, be obtained. Deviations from the standard DDR are also commonly encoded in a function  $\eta(z)$ , defined as

$$\eta(z) = \frac{d_L(z)}{d_A(z)(1+z)^2} = (1+z)^{\epsilon(z)}. \quad (5)$$

Similarly, deviations from the standard evolution of the CMB temperature with redshift can be parametrized phenomenologically by (Lima et al. 2000; Luzzi et al. 2009; Avgoustidis et al. 2012)

$$T(z) = T_0(1+z)^{1-\beta}, \quad (6)$$

where for simplicity it is assumed that violations of the standard behaviour are achromatic (they do not depend on the photons' wavelength) and approximately adiabatic, and therefore the spectrum of CMB radiation is still approximately a black body spectrum. A discussion of these assumptions can be found in Avgoustidis et al. (2016). It is important to stress that in models where the photon number is not conserved, the temperature-redshift relation and the DDR will both be violated. Therefore, in a broad range of models, the functions parameterizing these two possible violations will not be independent; defining a generic function  $f(z)$  encoding the violation of the temperature-redshift relation as

$$T(z) = T_0(1+z)f(z), \quad (7)$$

it is possible to show (Avgoustidis et al. 2012) that the DDR violation will then be

$$d_L(z) = d_A(z)(1+z)^2 f(z)^{3/2}. \quad (8)$$

Therefore, for the two simple parameterizations introduced above, the parameterized deviations from the standard model are related as

$$\epsilon = -\frac{3}{2}\beta. \quad (9)$$

In this work we focus on a specific class of mechanisms producing violations of Eq. (1) and Eq. (3), assuming that these are due to a change in the photon flux during the propagation from distant sources. Such mechanisms would affect the supernovae luminosity distance measures but not the determinations of the angular diameter distance. This means that probes of the latter (BAO) can be combined with supernova surveys to constrain deviations from photon number conservation.

Photon conservation can be violated by simple astrophysical effects or by exotic physics. Amongst the former we find, for instance, attenuation due to interstellar dust, gas and/or plasma. Such astrophysical mechanisms produce an effective opacity which would correspond to a positive value of the phenomenological parameter  $\epsilon$ . Most known sources of attenuation are expected to be clustered and can be typically constrained down to the 0.1% level (Ménard et al. 2008; More et al. 2009).

Unclassified sources of attenuation are more difficult to constrain. Grey dust (Aguirre 1999) was initially invoked to explain the observed dimming of Type Ia supernovae (SNIa) without resorting to cosmic acceleration. While this has been subsequently ruled out by observations (Aguirre & Haiman 2000; Bassett & Kunz 2004), it has been shown (Corasaniti 2006) that the effect of grey dust could cause an extinction as large as 0.08 mag at

$z = 1.7$ , thus potentially affecting dark energy parameter inference from future supernova surveys.

Concerning exotic physics explanations, a possible source of photon conservation violation is the coupling of photons to particles beyond the Standard Model of particle physics. Such couplings would mean that, while passing through the intergalactic medium, a photon could disappear, or even (re)appear, while interacting with such exotic particles, modifying the apparent luminosity of sources. Therefore, in this case we may in principle envisage both positive and negative values for  $\epsilon$ . In Avgoustidis et al. (2010) the mixing of photons with several such particles has been considered and constrained in three representative scenarios: scalars known as axion-like particles (Svrcek & Witten 2006), chameleons (Brax et al. 2010), and the possibility of mini-charged particles which have a tiny and unquantized electric charge (Holdom 1986; Batell & Gherghetta 2006). The implications of each of these three specific scenarios for the SNIa luminosity have been described by several authors (Csáki et al. 2002; Mörtzell et al. 2002; Burrage 2008; Ahlers 2009).

Finally, it is worth noting that any violations in photon conservation can be described as an opacity effect in the observed luminosity distance, which one can parameterize through a generic opacity parameter,  $\tau(z)$ , as

$$d_{L,\text{obs}}^2 = d_{L,\text{true}}^2 \exp[\tau(z)]. \quad (10)$$

Note that a negative  $\tau(z)$  allows for apparent brightening of light sources, as would be the case, for example, if exotic particles were also emitted from the source and converted into photons along the line of sight (see Burrage 2008). For specific models of exotic matter-photon coupling, such as axion-like particles, chameleons, and mini-charged particles, the function  $\tau(z)$  can be obtained in terms of the parameters of the model (Avgoustidis et al. 2010).

### 3. Analysis method

In this paper, we aim at obtaining constraints on possible deviations from the standard DDR, without assuming any specific model, from both current and mock data. For this reason we adopt two different approaches: on the one hand we parameterize the  $\epsilon(z)$  function, both as a constant and binning it in redshift, while on the other hand we also adopt a more general approach based on machine learning, reconstructing the function with genetic algorithms. In this section we review in detail the two approaches.

#### 3.1. Parameterized approach

A first simple way to constrain the cosmic DDR is to parameterize departures from the Etherington relation through a constant (redshift-independent) parameter  $\epsilon_0$ , i.e.

$$d_L(z) = (1+z)^{2+\epsilon_0} d_A(z), \quad (11)$$

with  $\epsilon_0 = 0$  being the standard limit. However, we are also interested in a possible redshift dependence of such departures, as many of the theoretical models discussed in Sect. 2 produce a redshift dependent modification of the DDR. Therefore, we take one step further by using the general form of Eq. (4). Choosing a specific model violating the Etherington relation would allow us to obtain  $\epsilon(z)$  in terms of the parameters of the chosen model. However, since the aim of this paper is not to constrain specific theories, in order not to make strong assumptions on the redshift

dependence of  $\epsilon(z)$ , we consider a simple binning of this function in two redshift bins, i.e.

$$\epsilon(z) = \begin{cases} \epsilon_0 & \text{if } z < z_*, \\ \epsilon_1 & \text{if } z \geq z_*, \end{cases} \quad (12)$$

where  $z_*$  is a transition redshift; we will comment on the choice of this redshift in the results section.

In order to constrain these two parameterizations, we implement them in a new likelihood module interfaced with the publicly available MCMC sampler Cobaya (Torrado & Lewis 2020), able to reconstruct the posterior distribution of cosmological parameters, using SnIa and BAO data coming from current surveys or from simulated datasets. SnIa data are compared with the theoretical predictions given by Eq. (4), while with BAO data we compare combinations of the Hubble parameter  $H(z)$  and of the standard angular diameter distance of Eq. (2).

We assume for this parameterized approach that the Universe expansion is well described by a flat  $\Lambda$ CDM model, with the late time evolution dominated by a cosmological constant with equation of state parameter  $w(z) = -1$ . Therefore, we sample through Cobaya  $\epsilon_0$  and  $\epsilon_1$ , parameterizing deviations from the standard DDR, alongside the total energy density of matter  $\Omega_{m,0}$ , and the Hubble constant  $H_0$ , using flat priors on these parameters. The assumption of a flat Universe implies that the energy density given by the cosmological constant  $\Lambda$  is  $\Omega_{\Lambda,0} = 1 - \Omega_{m,0}$ , neglecting the contribution of radiation energy density since we are analyzing low redshift data. Furthermore, we fix the baryon energy density to the mean obtained by Planck  $\Omega_{b,0}h^2 = 0.02225$  (Planck Collaboration: Aghanim et al. 2018). Abandoning the assumption of  $\Lambda$ CDM and allowing for free parameters describing the equation of state of the new dark energy component would impact the constraints on DDR violation parameters, with the possibility of introducing degeneracies between the parameters determining  $w(z)$  and  $\epsilon(z)$ ; we leave however the investigation of this possibility for future work.

### 3.2. Genetic algorithms

The Genetic Algorithms (GA) represent a class of machine learning methods that can be used for non-parametric reconstruction of data and are based on the notions of grammatical evolution, as expressed by the genetic operations of crossover and mutation. In particular, the GA mimic the principle of evolution through the implementation of natural selection; a group of individuals evolves over time under the influence of the stochastic operators of mutation, i.e. a random change in an individual, and crossover, i.e. the combination of different individuals to form offspring.

The probability that a member of the population will produce offspring, or in other terms its “reproductive success”, is assumed to be proportional to its fitness. The latter measures how accurately each individual of the population fits the data, here quantified through a  $\chi^2$  statistic (for more details on the GA and various applications to cosmology see Bogdanos & Nesseris 2009; Akrami et al. 2010; Nesseris & Shafieloo 2010; Nesseris & Garcia-Bellido 2012, 2013; Sapone et al. 2014; Arjona & Nesseris 2019, 2020; Arjona 2020), which is obtained following the same likelihood computation used in Sect. 3.1.

Qualitatively, the joint reconstruction of the SnIa and BAO data with the GA proceeds as follows. An initial population of functions is randomly chosen such that every member of the population contains initial guesses for both the luminosity distance

$d_L(z)$  and the duality parameter  $\eta(z)$ . At this point we also impose some physical priors, e.g. that the luminosity distance at  $z = 0$  is zero, but we make no assumption on a DE model. Then, each member’s fitness is calculated via a  $\chi^2$  statistic, using as input the SnIa and BAO data and their individual covariances. Subsequently, the mutation and crossover operators are applied to the best-fitting functions in every generation, chosen via tournament selection—see Bogdanos & Nesseris (2009) for more details. This process is then iterated thousands of times, so as to ensure convergence, and with different random seeds, so as not to bias the results due to a specific choice of the random seed.

After the GA code has converged, the final output is a pair of two continuous and differentiable functions of redshift that describe the luminosity distance  $d_L(z)$  and the duality parameter  $\eta(z)$  respectively. At every step the angular diameter distance is calculated following Eq. (5), while the Hubble parameter  $H(z)$  is calculated via differentiation of the latter assuming flatness. In the case of the current data we also numerically minimize the  $\chi^2$  at every step over the combination  $r_s(z_d)h$ , with  $r_s(z_d)$  the comoving sound horizon at the drag epoch and  $h = H_0/(100 \text{ km s}^{-1} \text{ Mpc}^{-1})$ , in order to avoid making any model assumptions for the BAO physics at early times.

To estimate the errors on the reconstructed functions we use an analytical approach developed by Nesseris & Garcia-Bellido (2012, 2013), where the errors are calculated via a path integral over the whole functional space that can be scanned by the GA. The GA path integral approach was extensively tested by Nesseris & Garcia-Bellido (2012) and found to be in excellent agreement with bootstrap Monte-Carlo error estimates.

In summary, using this approach we can reconstruct any cosmological function, for example the luminosity distance  $d_L(z)$  or the duality parameter  $\eta(z)$  that we consider here, by applying the GA to any dataset of choice. No assumptions on the specific cosmological model or the behaviour of DE need to be made, hence our results are independent from specific DDR violation models. Since in our case the best-fit is very close to  $\Lambda$ CDM and the errors are much larger than the effects of any possible model-bias in the covariances of the data, we can safely assume for the time being that these effects have a rather minimal impact on the whole minimization process.

Finally, for the numerical implementation of the GA used in this paper we use the publicly available code *Genetic Algorithms*<sup>1</sup>. In addition to performing a large number of GA runs with different random seed numbers, we have also required that all reconstructed functions, as well as their derivatives, are continuous in the range of redshifts we consider, in order to avoid spurious reconstructions and overfitting.

## 4. Analysis of currently available data

In order to constrain the deviation from the standard DDR, we need to analyze a set of data providing information on the luminosity and angular diameter distances. We focus therefore on currently available observations of SnIa and BAO.

The BAO data will provide information on the angular diameter distance  $d_A(z)$  and the Hubble parameter  $H(z)$ . We use here measurements of the ratio  $d_z$ , defined as

$$d_z \equiv \frac{r_s(z_d)}{D_V(z)}, \quad (13)$$

<sup>1</sup> <https://github.com/snesseris/Genetic-Algorithms>

where  $D_V$  is the volume averaged distance

$$D_V(z) = \left[ (1+z)^2 d_A^2(z) \frac{cz}{H(z)} \right]^{1/3}, \quad (14)$$

and  $r_s(z_d)$  is the comoving sound horizon at the drag epoch

$$r_s(z_d) = \frac{1}{H_0} \int_{z_d}^{\infty} \frac{c_s(z)}{H(z)/H_0} dz, \quad (15)$$

with  $c_s(z)$  the sound speed and  $z_d$  the redshift at the drag epoch (see Eq. 4 of Eisenstein & Hu 1998). In the  $\Lambda$ CDM model, Eq. (15) can be approximated as (see Eq. 26 of Eisenstein & Hu 1998)

$$r_s(z_d) \simeq \frac{44.5 \log\left(\frac{9.83}{\Omega_{m,0} h^2}\right)}{\sqrt{1 + 10(\Omega_{b,0} h^2)^{3/4}}} \text{ Mpc}. \quad (16)$$

Throughout this paper we will assume that this approximation holds in all our parameterized analyses. Moreover, as the data combination considered here cannot constrain  $\Omega_{b,0} h^2$ , we assume the value  $\Omega_{b,0} h^2 = 0.02225$  from Planck 2018 (Planck Collaboration: Aghanim et al. 2018). Notice that the constraints one can obtain through analysis of the BAO can depend significantly on this assumption, with different choices available on how to obtain prior information on  $r_s(z_d)$  (see e.g. Cuesta et al. 2015, for a detailed discussion on the role of  $r_s(z_d)$  assumptions in BAO analysis). For instance, a change of 1% in the value of  $\Omega_{b,0} h^2$  leads to a change of about 2% on the distance ratio  $d_z$ . The observational constraints, on the other hand, on the quantity given by Eq. (13), as well as on the Hubble distance  $D_H(z) = c/H(z)$ , that we consider here are provided by the surveys 6dFGS (Beutler et al. 2011), SDDS (Anderson et al. 2014), BOSS CMASS (Xu et al. 2012), WiggleZ (Blake et al. 2012), MGS (Ross et al. 2015), BOSS DR12 (Gil-Marín et al. 2016), DES (Abbott et al. 2019), Ly- $\alpha$  observations from Blomqvist et al. (2019), SDSS DR14 LRG (Bautista et al. 2018) and quasars observations from Ata et al. (2018). In the rest of the paper, we will refer to the combination of these datasets as BAO, for simplicity. We refer the reader to Appendix A for further details on how these datasets are combined together and a description of their likelihood.

On the other hand, the SNIa data provide information on the luminosity distance  $d_L(z)$ , as the measured observable is the apparent magnitude  $m(z)$  which can be expressed as

$$m(z) = M_0 + 5 \log_{10} \left( \frac{d_L(z)}{\text{Mpc}} \right) + 25, \quad (17)$$

where  $M_0$  is the intrinsic magnitude of the considered supernova. Such a quantity is completely degenerate with the Hubble constant  $H_0$ , thus, if no external information is provided, SNIa data are not able to constrain these two quantities. Here, we analyze the SNIa data using the likelihood expression from Appendix C in Conley et al. (2011), which already takes into account the marginalization of  $M_0$  and  $H_0$  from the SNIa analysis. The dataset we consider for the SNIa is the updated Pantheon compilation of 1048 points from Scolnic et al. (2018).

#### 4.1. Parameterized results

Using the surveys described above we can quantify the current constraining power on the DDR, both in the constant and binned cases of the  $\epsilon$  parameterization. In Table 1 we report both of these results, whereas in Fig. 1 we show the constraints obtained

from the considered observables, both separately and in combination. The contours shown here clarify how SNIa data are able to constrain  $\epsilon(z)$ , although the degeneracy between  $\Omega_{m,0}$  and the DDR parameters significantly limits the constraining power. The BAO data on the other hand, are not sensitive to  $\epsilon(z)$ , but are able to obtain tight constraints on the allowed matter density. Therefore, when the two datasets are combined the degeneracy between  $\Omega_{m,0}$  and  $\epsilon_0$ ,  $\epsilon_1$  is broken.

One may notice that the mean of the DDR parameters is positive, both in the constant and binned cases, and that the inclusion of BAO data shifts the constraints towards the standard cosmology limit  $\epsilon(z) = 0$ . Using alternative BAO combinations, producing different constraints on  $\Omega_{m,0}$ , can therefore lead to different results on  $\epsilon(z)$ ; this is crucial if one wants to connect the constraints to viable theoretical models producing the inferred violation of DDR, as the mechanisms leading to a positive or negative  $\epsilon(z)$  can be significantly different, as discussed in Sect. 2.

Considering the combined Pantheon+BAO constraints, in the constant  $\epsilon(z)$  case, the posterior distribution peaks at  $\epsilon_0 \neq 0$ ; however, within the  $1\sigma$  limit, the result is compatible with zero. The binned  $\epsilon(z)$  case shows a similar behaviour: both the first and second bin parameters, i.e.  $\epsilon_0$  and  $\epsilon_1$ , are compatible with zero at  $1\sigma$ . Furthermore, the errors on these two parameters are very similar, showing how current data provide similar constraining power in the two redshift bins considered here. This is due to the fact that the transition redshift  $z_*$ , fixed here to  $z_* = 0.9$ , lies roughly midway through the redshift range of the SNIa data, which are those sensitive to DDR parameters. It is important to stress here that throughout this analysis, we keep the transition redshift  $z_*$  fixed. Moreover, current data do not provide any hint for  $\epsilon_0 \neq \epsilon_1$ , as the constraints of both parameters are compatible with each other and therefore consistent with a constant  $\epsilon(z)$ . We analyzed the data also allowing for a free  $z_*$ ; however, as the data are compatible with a constant  $\epsilon(z)$ , no clear peak of the posterior distribution is present, with the two extreme cases  $z_* \approx 0$  and  $z_* \gtrsim 2$  providing the same result. Therefore, the posterior distribution is extremely difficult to sample with the MCMC algorithm used here, and we decide to present here only the analysis where  $z_*$  is fixed.

In particular, using both the current SNIa and BAO data, we find  $\epsilon_0 = 0.013 \pm 0.029$ , while, when the binned approach is used, we find  $\epsilon_1 = 0.009 \pm 0.030$  and  $\epsilon_0 = 0.015^{+0.027}_{-0.031}$ . The former may be compared to the analysis by Avgoustidis et al. (2010), where  $\epsilon_0$  was found to be  $\epsilon_0 = -0.04^{+0.08}_{-0.07}$  (all of these being at the 68% confidence level).

Finally, we show in Fig. 2 the reconstructed trend of  $\eta(z)$ , whose values at different redshifts are obtained as a derived parameter using Eq. (5). As can be seen, the reconstruction is in agreement with  $\Lambda$ CDM within the errors.

#### 4.2. GA results

In order to obtain constraints on the violation of the DDR without assuming any specific trend in redshift for  $\epsilon(z)$ , we employ here the GA approach described in Sect. 3.2, applied simultaneously to the currently available SNIa and BAO data. We find that a joint fit with the GA to both data sets gives a competitive fit with respect to the  $\Lambda$ CDM model. In particular, after applying the GA we find a best-fit of  $\chi^2_{\text{min,GA}} = 1041.510$  for  $r_s(z_d) = 100.360 \text{ Mpc}/h$ . Concerning the  $\Lambda$ CDM model, we obtain a minimum value of  $\chi^2_{\text{min},\Lambda\text{CDM}} = 1045.696$ , for  $1048 + 12 = 1060$  data points (1048 from the SNIa and 12 from the BAO respectively), for the best-fit matter density parameter

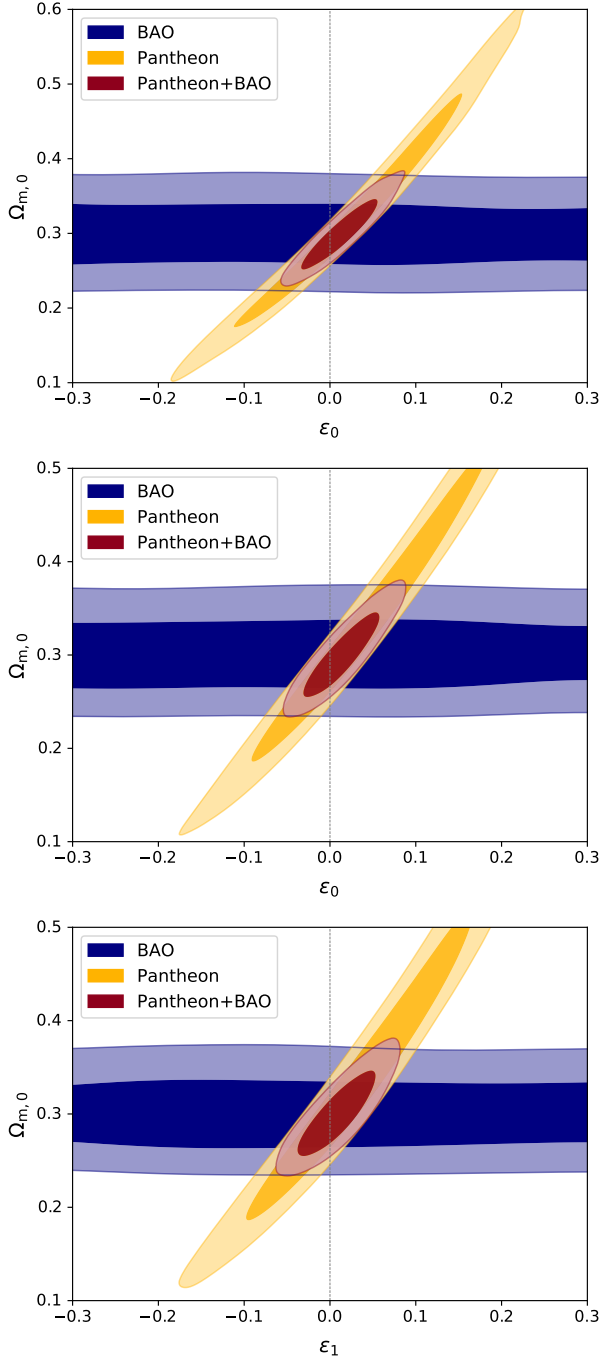


**Fig. 1.** 2D contours on  $\Omega_{m,0}$ ,  $\epsilon_0$  and  $\epsilon_1$ , using currently available data for BAO (blue), SnIa (yellow) and the combination of the two (red). These results refer to the constant (top panel) and binned (central and bottom panels)  $\epsilon(z)$  cases.

$\Omega_{m,0} = 0.297 \pm 0.018$  and  $H_0 = 66.7 \pm 1.0$  km/s/Mpc. Overall, the GA provides a better fit to the data, with  $\Delta\chi^2 = 4.187$ , compared to the  $\Lambda$ CDM model.

As mentioned before, the output of the GA is an analytical function, but in most cases the exact expression is both cumbersome and not informative. Though, in this case we were able to find a compact expression for the GA reconstruction of the  $\eta(z)$  parameter, given by

$$\eta(z) = (1+z)^{0.0294-0.0002z^4}. \quad (18)$$

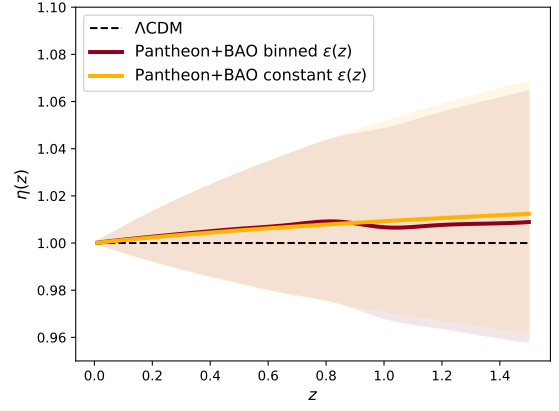


**Fig. 2.** Reconstruction with current SnIa and BAO data of the  $\eta(z)$  function at different redshifts, as derived parameters using Eq. (5). The mean function is shown as a solid line, while the shaded area represents the 68% confidence region. The red color shows the result in the binned  $\epsilon(z)$  case, while yellow refers to the constant case

**Table 1.** Mean values and marginalized 68% confidence level errors obtained from currently available data on the cosmological parameters  $\Omega_{m,0}$  and  $H_0$  (in units of  $\text{km s}^{-1} \text{Mpc}^{-1}$ ), and on the DDR parameters  $\epsilon_0$  and  $\epsilon_1$  (if present).

		constant $\epsilon(z)$	binned $\epsilon(z)$
parameter	probe		
$H_0$	BAO	$66.6^{+1.3}_{-1.4}$	$66.7 \pm 1.3$
	SnIa	unconstrained	unconstrained
	SnIa+BAO	$66.6 \pm 1.3$	$66.6 \pm 1.3$
$\Omega_{m,0}$	BAO	$0.300^{+0.027}_{-0.036}$	$0.302^{+0.027}_{-0.035}$
	SnIa	$0.329^{+0.094}_{-0.12}$	$0.357^{+0.090}_{-0.14}$
	SnIa+BAO	$0.301^{+0.028}_{-0.034}$	$0.301^{+0.026}_{-0.033}$
$\epsilon_0$	BAO	unconstrained	unconstrained
	SnIa	$0.030 \pm 0.088$	$0.056^{+0.087}_{-0.10}$
	SnIa+BAO	$0.013 \pm 0.029$	$0.015^{+0.027}_{-0.031}$
$\epsilon_1$	BAO	—	unconstrained
	SnIa	—	$0.046 \pm 0.089$
	SnIa+BAO	—	$0.009 \pm 0.030$

As can be seen, the value of  $\epsilon(z)$  derived from Eq. (18) is compatible with the one derived in the parameterized approach. Moreover, the value predicted from the GA has a redshift dependence  $O(z^4)$ , which is only important at high redshifts as the coefficient is sufficiently small, albeit negative. This is also in agreement with the fact that the parameterized approach finds a value for  $\epsilon$  that is smaller in the second bin with respect to the first. Finally, unfortunately the GA reconstructions for the luminosity distance or the Hubble parameter are far too unwieldy, so we refrain from reporting them here.

Having performed the fit to the data, we now show in the left panel of Fig. 3 the reconstruction of the distance modulus  $\mu(z) = m(z) - M_0$ , rescaled by the  $\Lambda$ CDM best-fit with  $\Omega_{m,0} = 0.297 \pm 0.018$ . By definition, the dashed line at zero corresponds to the best-fit  $\Lambda$ CDM, the red line is the GA fit and the shaded region corresponds to the  $1\sigma$  GA errors. The constraints on the distance modulus are tighter at low redshifts  $z \in [0, 0.5]$  where we have the bulk of the BAO and SnIa data points, but also due to the fact that the distance modulus  $\mu(z)$  is a function of the luminosity distance  $d_L(z)$  and as a result it naturally converges to a fixed value at  $z = 0$ .

In the right panel Fig. 3 we show the duality parameter  $\eta(z)$  of Eq. (5), obtained through the GA reconstruction of  $d_A(z)$  from the BAO data and the luminosity distance  $d_L(z)$  based on the Pantheon SNIa set. The dashed line at unity is  $\Lambda$ CDM, the red line is the GA fit and the shaded region corresponds to the  $1\sigma$  GA errors. As can be seen, the reconstruction of  $\eta(z)$  is compatible with unity at the  $1\sigma$  level, hence the GA does not detect any statistically significant deviations from the  $\Lambda$ CDM model with the currently available data.

## 5. SNIa and BAO mock data

Upcoming surveys have the potential to improve the constraining power on deviations from the standard DDR, thanks to improved data both for SNIa and LSS observations, where the latter provide information on the angular diameter distance and the Hubble parameter. We are interested therefore in forecasting how future surveys will constrain the DDR, and in order to do so we create simulated datasets for both SNIa and BAO measurements.

For these simulations, we use the fiducial cosmology shown in Table 2, i.e. the same used in EC19, where we assume no violation of the DDR. Using these values we create our fiducial luminosity and angular diameter distances, as well as the redshift evolution of the Hubble parameter. Once the fiducial cosmological quantities are computed, we create our mock data following the specification of forthcoming surveys.

### 5.1. SNIa surveys

Here we consider two different surveys. On the one hand, we simulate future observations based on the specifications of the LSST, which we assume will observe a number of SNIa  $N_{\text{SNIa}} = 8800$  in the redshift range  $z \in [0.1, 1.0]$ . We then extend the redshift range of our SNIa dataset by including simulated observations for the proposed *Euclid* DESIRE survey (Laureijs et al. 2011; Astier et al. 2014), thus including 1700 additional data points in the range  $z \in [0.7, 1.6]$ . For both surveys, we assume the redshift distributions shown in Astier et al. (2014), and we further assume that the two are not correlated<sup>2</sup>. For each event, we simulate an observational error  $\sigma_{\text{tot},i}$  given by

$$\sigma_{\text{tot},i}^2 = \delta\mu_i^2 + \sigma_{\text{flux}}^2 + \sigma_{\text{scat}}^2 + \sigma_{\text{intr}}^2, \quad (19)$$

where the flux, scatter, and intrinsic contributions are the same for each event ( $\sigma_{\text{flux}} = 0.01$ ,  $\sigma_{\text{scat}} = 0.025$ , and  $\sigma_{\text{intr}} = 0.12$  respectively), and we add an error contribution on the distance modulus  $\mu = m - M$ , which evolves linearly in redshift

$$\delta\mu = e_M z, \quad (20)$$

where  $e_M$  is drawn from a Gaussian distribution with vanishing mean and  $\sigma(e_M) = 0.01$  (see Gong et al. 2010; Astier et al. 2014).

Note that while the effects of lensing by foreground structures are already included in the Pantheon data by incorporating an error  $\sigma_{\text{lens}}$  (see Scolnic et al. 2018), here we have not included this error in our mocks as it has a very weak redshift dependence and is subdominant with respect to the intrinsic distance scatter of every point of  $\sim 0.12\text{mag}$ . Thus, we do not expect it to affect our results.

<sup>2</sup> Notice that the DESIRE survey is not a guaranteed output of *Euclid*. Here we include this in the analysis as a possible survey extending the redshift range of LSST. Such a survey will be crucial for performing the GA reconstruction at higher redshifts.

### 5.2. LSS surveys

As one of the main objectives of this paper is to forecast the constraints achievable on DDR with *Euclid*, we simulate BAO data from this survey using the Fisher matrix technique, following the same strategy used in EC19 for the spectroscopic survey.

Since in this work we are interested in using precise measurements of the Hubble parameter and the angular diameter distance to test the DDR, we will focus on the spectroscopic *Euclid* survey. Through this, *Euclid* will be capable of exploring the galaxy power spectrum in a range of redshifts  $z \in [0.95, 1.75]$ . As described in EC19, the main targets are  $H_\alpha$  emitters, and the survey is able to measure up to 30 million spectroscopic redshifts with an error of  $\sigma_z = 0.001(1+z)$  (Pozzetti et al. 2016). The main observable is the galaxy power spectrum which contains information about the galaxy bias, the anisotropies due to redshift space distortions, the residual shot noise, the redshift uncertainty and the distortion due to the Alcock-Paczynski effect. Furthermore, the matter power spectrum has been modulated with non-linear effects which distort the shape of the power spectrum (Wang et al. 2013).

With respect to EC19, in this work we use a different binning scheme. Instead of 4 redshift bins we divide the observed redshift range in 9 equally spaced bins of width  $\Delta z = 0.1$ . The galaxy number density  $n(z)$ , in units of  $\text{Mpc}^{-3}$  and the galaxy bias  $b(z)$  have been obtained rebinning those of EC19, finding:

$$\begin{aligned} n(z) &= \{2.04, 2.08, 1.78, 1.58, 1.39, 1.15, 0.97, 0.7, 0.6\} \times 10^{-4} \\ b(z) &= \{1.42, 1.5, 1.57, 1.64, 1.71, 1.78, 1.84, 1.90, 1.96\}. \end{aligned}$$

The different binning choice allows obtaining more data points from this survey, which improves the machine learning analysis we perform through GA. Nevertheless, we have compared the final bounds obtained on cosmological parameters with this choice against those of EC19, finding no significant effect.

Using these specifications, we follow the procedure described in EC19 to obtain the Fisher matrix for the full set of cosmological parameters, i.e.: 4 shape parameters  $\{\omega_m = \Omega_{m,0}h^2, h, \omega_b = \Omega_{b,0}h^2, n_s\}$ , 2 non-linear parameters  $\{\sigma_8, \sigma_v\}$  and 5 redshift dependent parameters  $\{\ln d_A, \ln H, \ln f\sigma_8, \ln b\sigma_8, P_s\}$  evaluated in each redshift bin. Using such an approach, we obtain the expected errors from this survey on the angular diameter distance  $d_A(z)$  and the Hubble parameter  $H(z)$  in each of the 9 redshift bins, while marginalizing over all the other free parameters. The results of the Fisher matrix procedure are in principle dependent on the chosen fiducial cosmology, but we assume here that this dependence is negligible.

In Sect. 4 we have shown how for our parameterized approach we need to break the degeneracy between the DDR parameters and  $\Omega_{m,0}$ , and the BAO measurements from *Euclid* will be able to measure this parameter. However, we are able to use our GA reconstruction approach only in the redshift range where both SNIa and BAO data are available. Using only *Euclid* alongside LSST and DESIRE would therefore limit the validity of such an approach to only the redshift range  $z \in [0.95, 1.6]$ . In order to be able to reconstruct the DDR functions at all redshift for which we have SNIa data available, we complement the redshift range of *Euclid* by exploiting the extended redshift range of the DESI survey, which started operations at the end of 2019 and will obtain optical spectra for tens of millions of galaxies and quasars up to redshift  $z \sim 4$ .

Such spectra will enable BAO and redshift-space distortion cosmological analyses. We use here the official DESI forecasts on future constraints for both  $H(z)$  and  $d_A(z)$  (DESI Collaboration: Aghamousa et al. 2016). These have been obtained with



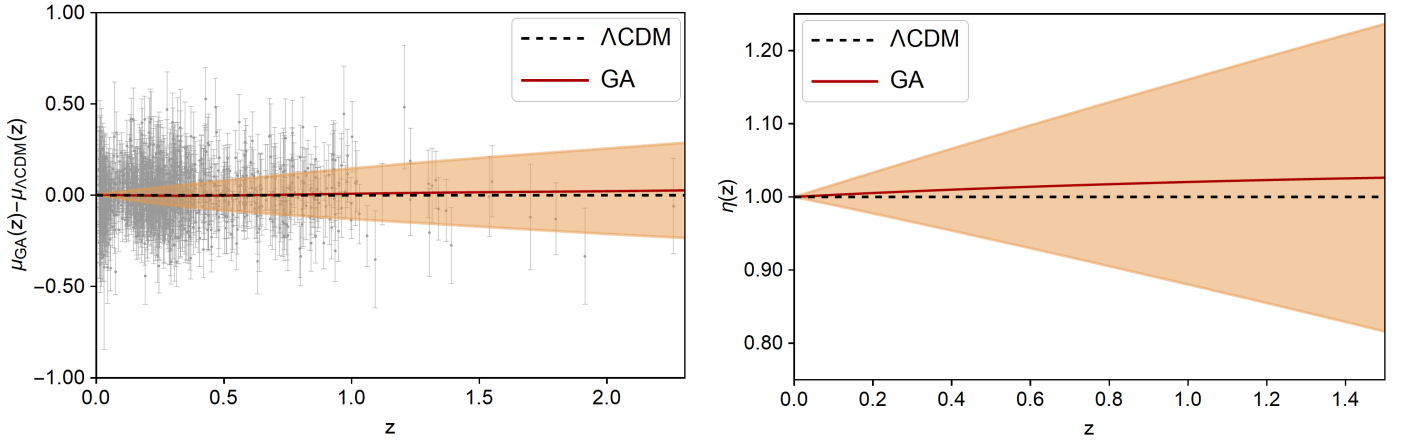


**Fig. 3.** Left: The distance modulus based on the Pantheon SNIa set, rescaled by the best-fit  $\Lambda$ CDM model ( $\Omega_{m,0} = 0.297 \pm 0.018$ ). The dashed line at zero corresponds to  $\Lambda$ CDM, the red line is the GA fit and the shaded region corresponds to the  $1\sigma$  GA errors. Right: The duality relation  $\eta(z)$  for the GA reconstruction of  $d_A(z)$  from the BAO data and the luminosity distance  $d_L(z)$  based on the Pantheon SNIa set. The dashed line at unity is  $\Lambda$ CDM, the red line is the GA fit and the shaded region is the  $1\sigma$  GA errors.

**Table 2.** The parameter values for the fiducial model we used for the mock. The values used follow the fiducial of EC19.  $H_0$  is shown in units of  $\text{km s}^{-1} \text{Mpc}^{-1}$ .

$M_0$	$\Omega_{m,0}$	$\Omega_{b,0}h^2$	$H_0$	$w_0$	$w_a$	$\epsilon_0$	$\epsilon_1$
-19.3	0.32	0.02225	67	-1	0	0	0

a Fisher matrix formalism, following Font-Ribera et al. (2014), which includes the “broadband” galaxy power, i.e. measurements of the power spectrum as a function of redshift, wavenumber, and angle with respect to the line of sight. As for the *Euclid* approach described above, this encodes all the available information from the two-point clustering and not just the position of the BAO peak. In more detail, we consider the DESI baseline survey, which consists of a coverage of  $14\,000 \text{ deg}^2$  and the four different types of DESI targets: bright galaxies (BGs), luminous red galaxies (LRGs), emission line galaxies (ELGs), and quasars. The DESI forecast measurements will cover the redshift range  $z \in [0.05, 3.55]$ , but their precision will also depend on the target population. The BGs will cover the redshift range  $z \in [0.05, 0.45]$  in 5 equispaced redshift bins, the LRGs and ELGs will focus on  $z \in [0.65, 1.85]$  with 13 equispaced redshift bins, while the Ly- $\alpha$  forest quasar survey will cover  $z \in [1.96, 3.55]$  with 11 equispaced redshift bins. We further assume these measurements to be uncorrelated.

In the following, when using the combination of BAO data from *Euclid* and DESI, as we do not consider correlations between these surveys, we will only include DESI observations that do not overlap in redshift with the *Euclid* measurements. Moreover, since we only have SNIa data from LSST+DESIRE up to  $z = 1.6$ , we will only include in the analysis the full BGs survey, and the LRGs and ELGs up to  $z = 0.9$ , thus including no information from observations of the Ly- $\alpha$  forest.

## 6. Forecast results

Following the approach described in Sect. 3, we constrain the cosmological and DDR parameters using our mock data for SNIa and BAO. In Table 3 we show the mean values and errors for the free parameters of the analysis, when using the data from LSST+DESIRE for SNIa and from *Euclid*+DESI for BAO, for

both the constant and binned  $\epsilon(z)$ . In Fig. 4 instead we compare the results of the combination of these surveys with those obtained using current data, and to what can be achieved using only the BAO survey from *Euclid*. This is to be compared with Fig. 54 in Amendola et al. (2018), whose forecast was for *Euclid* (with the specifications foreseen at the time) plus a Stage IV (SNAP-like) SNIa mission: the achieved constraints are compatible with what we find here. In summary,  $\epsilon_0$  and  $\epsilon_1$  are now constrained with an error smaller than  $10^{-2}$ , improving the sensitivity of current constraints by about a factor of  $\approx 6$ . Notice that here we are not considering one of the two primary probes of *Euclid*, i.e. cosmic shear. Adding the information brought by such a probe would further constrain the value of  $\Omega_{m,0}$ , thus resulting in even tighter bounds on the DDR parameters  $\epsilon_0$  and  $\epsilon_1$ .

As can be seen in Fig. 4 the addition of DESI to the combination of LSST+*Euclid* does not improve the constraints significantly. This could be somewhat surprising, as one would expect that, given the complementarity in redshift range between the two surveys, the combination of the two would provide improvements in the constraints. Our results show instead that the constraining power on  $\Omega_{m,0}$  from *Euclid* alone is the one dominating the constraints and therefore driving the breaking of the degeneracy between  $\Omega_{m,0}$  and  $\epsilon(z)$  parameters. While the  $z = 0.9$  cut we perform to avoid an overlap of the two BAO surveys is not *per se* behind this effect, we do expect that the use of the full DESI data (specifically the high-redshift galaxy and the Ly- $\alpha$  data) would lead to a stronger improvement in the constraints. However, in order to investigate this further, correlations between the two mock datasets should be properly taken into account, an analysis that is outside the scope of this paper.

Furthermore, in Fig. 5 we show  $\eta(z)$  obtained using Eq. (5) with the parameterized approach constraints; we find that these are significantly improved with respect to current results, showing the high constraining power that can be reached using upcoming surveys.

As a final analysis, we apply the GA reconstruction method to the mock BAO and SNIa data. In the left panel of Fig. 6 we show the reconstruction of the angular diameter distance  $d_A(z)$  with the GA approach using the mock BAO *Euclid* data. The dashed black line is the best-fit  $\Lambda$ CDM model, the solid red line is the GA fit to the *Euclid* BAO data, while the shaded region corresponds to the  $1\sigma$  GA errors. In the central panel of Fig. 6 we show the GA reconstruction of the distance modulus  $\mu(z)$



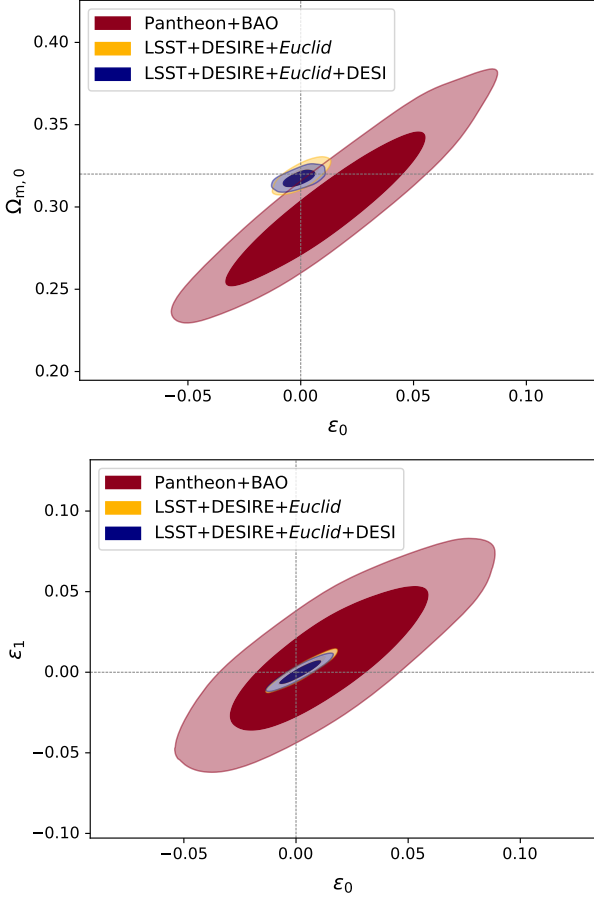


**Fig. 4.** 2D contours on  $\Omega_{m,0}$ ,  $\epsilon_0$  and  $\epsilon_1$ , using the combination of BAO and SnIa dataset given by currently available data (red contours), LSST supernovae and *Euclid* BAO data (yellow contours), and the combination of LSST supernovae with BAO forecasts coming from the combination of *Euclid* and DESI (blue contours). These results refer to the constant (top panel) and binned (bottom panel)  $\epsilon(z)$  cases. The dashed lines identify the limit  $\epsilon(z) = 0$ .

**Table 3.** Mean values and marginalized 68% confidence level errors obtained from mock LSST (SnIa), *Euclid* (SnIa and BAO) and DESI (BAO) data on the cosmological parameters  $\Omega_{m,0}$  and  $H_0$  (in units of  $\text{km s}^{-1} \text{Mpc}^{-1}$ ), and on the DDR parameters  $\epsilon_0$  and  $\epsilon_1$  (if present).

param.	probe	const. $\epsilon(z)$	binned $\epsilon(z)$
$H_0$	BAO	$67.13 \pm 0.25$	$67.14 \pm 0.25$
	SnIa	unconstrained	unconstrained
	SnIa+BAO	$67.14 \pm 0.26$	$67.15 \pm 0.26$
$\Omega_{m,0}$	BAO	$0.3175 \pm 0.0034$	$0.3174 \pm 0.0034$
	SnIa	$0.259 \pm 0.077$	$0.281 \pm 0.096$
	SnIa+BAO	$0.3174^{+0.0032}_{-0.0036}$	$0.3172 \pm 0.0035$
$\epsilon_0$	BAO	unconstrained	unconstrained
	SnIa	$-0.060^{+0.090}_{-0.062}$	$-0.040^{+0.11}_{-0.071}$
	SnIa+BAO	$-0.0008 \pm 0.0049$	$0.0019 \pm 0.0061$
$\epsilon_1$	BAO	—	unconstrained
	SnIa	—	$-0.042^{+0.11}_{-0.068}$
	SnIa+BAO	—	$0.0001 \pm 0.0049$

using the LSST+DESIRE simulated data rescaled by the best-fit  $\Lambda$ CDM, with the latter corresponding to the dashed line at

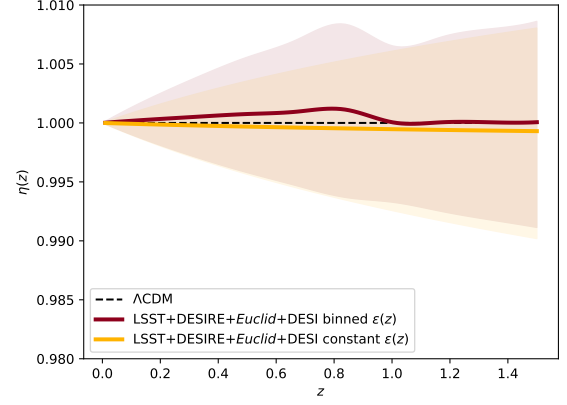


**Fig. 5.** Reconstruction with future SnIa and BAO data of the  $\eta(z)$  function at different redshifts, as derived parameters using Eq. (5). The mean function is shown as a solid line, while the shaded area represents the 68% confidence region. The red color shows the result in the binned  $\epsilon(z)$  case, while yellow refers to the constant case.

zero. Similarly to the left panel, the red line is the GA fit and the shaded region corresponds to the  $1\sigma$  GA errors. For clarity, we only show 1000 out of the total  $\sim 10\,000$  SnIa points we include in our mock dataset.

Finally, in the right panel of Fig. 6 we show the reconstruction of the  $\eta(z)$  function, which is obtained from the joint GA reconstruction of  $d_A(z)$  and  $d_L(z)$ . It is immediately clear that such a reconstruction is limited if performed using *Euclid* BAO data only: the lack of  $d_A(z)$  measurements for  $z < 0.9$  forces the method to be applied only in the redshift range  $z \in [0.9, 1.6]$ . Despite this, as can be seen in all panels of Fig. 6, the GA reconstruction for the mock *Euclid* BAO recovers the correct fiducial model in all three cases and in particular, it provides very tight constraints on both the angular diameter distance and the duality parameter  $\eta(z)$ . Specifically, comparing with the right panel of Fig. 3, we can see that with the GA approach, *Euclid* now brings roughly a factor of three improvement compared to the current data with a non-parametric approach.

We also consider the added benefit on the reconstruction brought by DESI BAO data, which cover, as mentioned earlier, the redshift range  $z \in [0, 0.9]$ . In Fig. 7 we show the reconstruction of the duality relation  $\eta(z)$  (left) and the  $\epsilon(z)$  parameter (right) when the full data combination of *Euclid* and DESI is considered. We find that, as in the case of the parameterized results, the addition of DESI to the combination of LSST+*Euclid* does not improve the constraints significantly, however in this case we can now cover a wider redshift range. The GA can then recover the fiducial model  $\eta(z) = 1$  with a 1% error at  $z = 0.2$  and a 5% error at  $z = 1$ , while the parameter  $\epsilon(z)$ , obtained inverting Eq. (5), can be measured in a model-independent fashion, with an error between 0.05 and 0.07 over the redshift range covered by the data.

## 7. Conclusions

In this work, we have constrained deviations from the standard Distance Duality Relation using current and forecast data; for the latter, we focused mainly on the constraints achievable through synergies between *Euclid* and contemporary surveys, both for SnIa and BAO. We have discussed in Sect. 2 several physical mechanisms that can lead to a violation of the DDR, both of as-

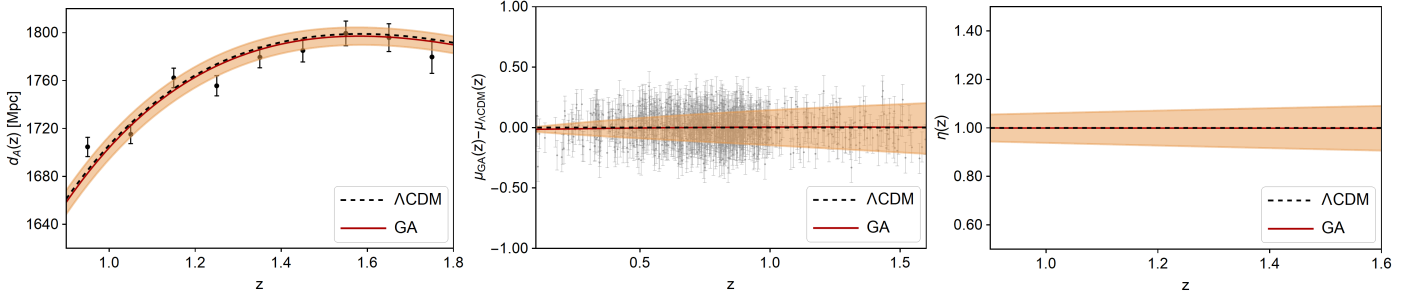


**Fig. 6.** Left: The reconstruction of the angular diameter distance  $d_A(z)$  from the mock *Euclid* data with the GA approach. The dashed black line is  $\Lambda$ CDM, the solid red line is the GA fit and the shaded region corresponds to the  $1\sigma$  GA errors. Center: Results on the distance modulus  $\mu(z)$  from the mock *Euclid* +LSST+DESIRE data with the GA approach. The dashed line at zero is  $\Lambda$ CDM, the red line is the GA fit and the shaded region corresponds to the  $1\sigma$  GA errors. For clarity, we only show one thousand of the total SNIa points. Right: The reconstruction of the  $\eta(z)$  parameter in the range  $z \in [0.9, 1.6]$ . In all cases the error bars of the data points correspond to  $1\sigma$  uncertainty.

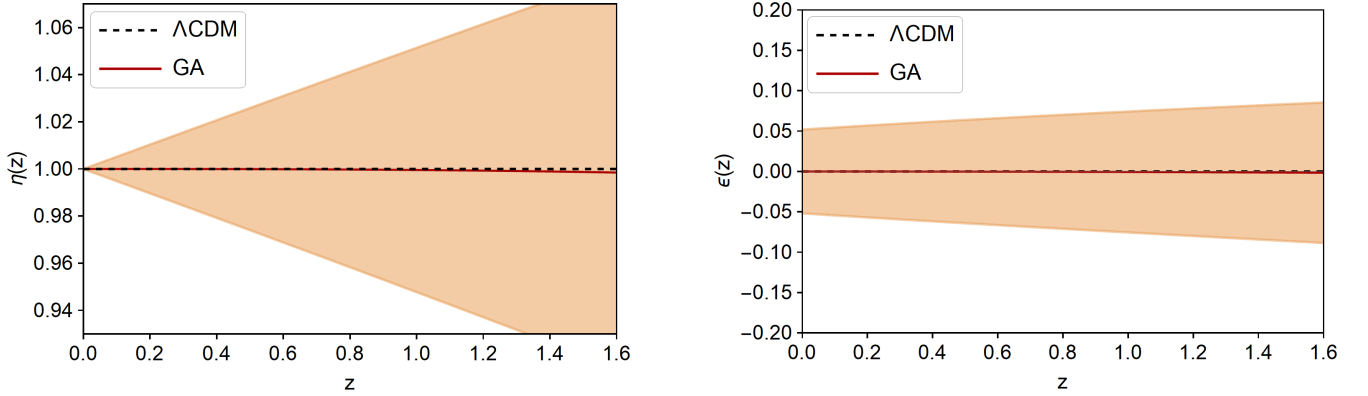


**Fig. 7.** Left: The duality relation  $\eta(z)$  for the GA reconstructions for the LSST+DESIRE SNIa data and *Euclid* plus DESI BAO mocks. Right: The reconstruction of the  $\epsilon(z)$  parameter, calculated via  $\epsilon(z) = \frac{\ln \eta(z)}{\ln(1+z)}$ , is found to be consistent with the fiducial value  $\epsilon(z) = 0$  within the errors. In both cases the GA reconstruction is the red line, while the shaded region corresponds to the  $1\sigma$  errors.

trophysical and beyond the standard model origin. For this reason, while we exploited a commonly used parametric approach to constrain the DDR breaking function  $\epsilon(z)$ , we also used a fully agnostic reconstruction through Genetic Algorithms. The latter approach allows us to obtain constraints without any assumption on the redshift trend of possible deviations from the standard theory.

In the parametric case, within the assumption of a flat  $\Lambda$ CDM expansion and using the value of  $\Omega_{b,0}h^2$  measured by Planck, we found that current SNIa data loosely constrain the deviation from the  $\epsilon(z) = 0$  limit, due to the degeneracy between the DDR parameters and the total matter energy density  $\Omega_{m,0}$ . Such a degeneracy is broken when including BAO data; these are not sensitive to violations of DDR, but tightly constrain  $\Omega_{m,0}$ , thus yielding tight constraints on the parameterized  $\epsilon(z)$ . The results obtained with the combination of SNIa and BAO data show that the standard DDR is within  $\approx 1\sigma$ , and the results are compatible with a constant  $\epsilon(z)$ .

In the case of the machine learning reconstruction, we found that the GA can provide robust constraints in line with the parametric approach, albeit with somewhat larger uncertainties. This is due to the fact that the GA is non-parametric, thus it provides broader and theory-agnostic constraints. Specifically, we found that in the case of the currently available data, the reconstruction of the duality parameter  $\eta(z)$  was fully consistent with the parametric approach and with unity.

Using the same fiducial cosmology assumed in EC19, we have then created simulated data for upcoming surveys; we focused mainly on the BAO data achievable with *Euclid*, and on

the possible SNIa survey DESIRE that might be provided by this satellite. We complemented the redshift range of *Euclid* forecast data with contemporary surveys, i.e. LSST for SNIa and DESI for BAO.

Analyzing these mock data through the parameterized approach, we found an improvement of a factor  $\approx 6$  with respect to current results when the combination of SNIa and BAO is considered (see Table 3). We have also shown in Fig. 5 how such constraints translate into a redshift trend for the  $\eta(z)$  function, highlighting how the use of mock data significantly improve the bounds on this functions, which is now constrained to vary less than 1% from the fiducial assumption of  $\eta(z) = 1$ .

Using the GA with the mock data, we reconstructed the duality parameter  $\eta(z)$  and we have shown how synergies of *Euclid* with other galaxy surveys are crucial in order to be able to use such an approach over an extended range in redshift. With the data combinations considered here we found that the GA can recover the fiducial model  $\eta(z) = 1$  with an error of 1% at  $z = 0.2$  and of 5% at  $z = 1$ , as shown in Fig. 7, and with an improvement of roughly a factor of three over the current DDR constraints in the same redshift range. This somewhat less constraining result, compared to the parameterized approach, is mainly due to the completely model-independent and theory-agnostic approach employed here, despite the joint fitting of the SNIa and BAO data.

In summary, our paper highlighted the benefits of synergies between the *Euclid* BAO survey and external probes in constraining physics beyond the standard model, which could manifest itself through violations of the DDR. In particular, we have

demonstrated that such a BAO survey will make it possible to constrain deviations from the DDR at an unprecedented level in the near future using parameterized approaches, while it will also reach a high enough sensitivity to employ model-independent approaches that allow an agnostic reconstruction of possible deviations from the standard DDR.

**Acknowledgements.** We are grateful to P. Astier for useful discussions and to T. Baker, G. Castignani and P. Ntelis for comments on the manuscript. MM has received the support of a fellowship from “la Caixa” Foundation (ID 100010434), with fellowship code LCF/BQ/PI19/11690015, and the support of the Spanish Agencia Estatal de Investigación through the grant “IFT Centro de Excelencia Severo Ochoa SEV-2016-0597”. The work of CJM was financed by FEDER—Fundo Europeu de Desenvolvimento Regional funds through the COMPETE 2020—Operational Programme for Competitiveness and Internationalisation (POCI), and by Portuguese funds through FCT - Fundação para a Ciência e a Tecnologia in the framework of the project POCI-01-0145-FEDER-028987. SN acknowledges support from the research project PGC2018-094773-B-C32, the Centro de Excelencia Severo Ochoa Program SEV-2016-059 and the Ramón y Cajal program through Grant No. RYC-2014-15843. DS acknowledges financial support from the Fondecyt Regular project number 1200171. IT acknowledges support from the Spanish Ministry of Science, Innovation and Universities through grant ESP2017-89838-C3-1-R, and the H2020 programme of the European Commission through grant 776247. AA acknowledges support from the Science and Technology Facilities Council (STFC) grant ST/P000703/1. VY acknowledges funding from the European Research Council (ERC) under the European Union’s Horizon 2020 research and innovation programme (grant agreement No. 769130).

The Euclid Consortium acknowledges the European Space Agency and the support of a number of agencies and institutes that have supported the development of *Euclid*, in particular the Academy of Finland, the Agenzia Spaziale Italiana, the Belgian Science Policy, the Canadian Euclid Consortium, the Centre National d’Etudes Spatiales, the Deutsches Zentrum für Luft- und Raumfahrt, the Danish Space Research Institute, the Fundação para a Ciência e a Tecnologia, the Ministerio de Economía y Competitividad, the National Aeronautics and Space Administration, the Nederlandse Onderzoekschool Voor Astronomie, the Norwegian Space Agency, the Romanian Space Agency, the State Secretariat for Education, Research and Innovation (SERI) at the Swiss Space Office (SSO), and the United Kingdom Space Agency. A detailed complete list is available on the *Euclid* web site (<http://www.euclid-ec.org>).

## Appendix A: The current BAO data

Here we describe the currently available BAO data we use in our analysis. In particular, we use the measurements from 6dFGS (Beutler et al. 2011), SDDS (Anderson et al. 2014), BOSS CMASS (Xu et al. 2012), WiggleZ (Blake et al. 2012), MGS (Ross et al. 2015) and BOSS DR12 (Gil-Marín et al. 2016), DES (Abbott et al. 2019), Lya (Blomqvist et al. 2019), DR14 LRG (Bautista et al. 2018) and quasars (Ata et al. 2018).

The data provided by these surveys are described by the function  $d_z$ , defined in Sect. 4. The 6dFGS and WiggleZ BAO data are

$$\begin{array}{ccc} z & d_z & \sigma_{d_z} \\ 0.106 & 0.336 & 0.015 \\ 0.44 & 0.073 & 0.031 \\ 0.6 & 0.0726 & 0.0164 \\ 0.73 & 0.0592 & 0.0185 \end{array} \quad (\text{A.1})$$

with their inverse covariance matrix given by

$$C_{ij}^{-1} = \begin{pmatrix} 4444.4 & 0 & 0 & 0 \\ 0 & 1040.3 & -807.5 & 336.8 \\ 0 & -807.5 & 3720.3 & -1551.9 \\ 0 & 336.8 & -1551.9 & 2914.9 \end{pmatrix}, \quad (\text{A.2})$$

and with the  $\chi^2$  being

$$\chi_{6dFGS,Wig}^2 = V^i C_{ij}^{-1} V^j, \quad (\text{A.3})$$

and the data vector  $V^i = d_{z,i} - d_z(z_i, \Omega_{m,0})$ .

The BAO measurements from MGS and SDSS (LOWZ and CMASS samples) are given by  $D_V/r_s = 1/d_z$  via

$$\begin{array}{ccc} z & 1/d_z & \sigma_{1/d_z} \\ 0.15 & 4.46567 & 0.168135 \\ 0.32 & 8.62 & 0.15 \\ 0.57 & 13.7 & 0.12 \end{array} \quad (\text{A.4})$$

and the  $\chi^2$  is then

$$\chi_{MGS,SDSS}^2 = \sum_i \left( \frac{1/d_{z,i} - 1/d_z(z_i, \Omega_{m,0})}{\sigma_{1/d_{z,i}}} \right)^2. \quad (\text{A.5})$$

The BAO data from DES is of the form  $d_A(z)/r_s$  with the data vector  $(z, d_A(z)/r_s, \sigma) = (0.81, 10.75, 0.43)$  and the  $\chi^2$  being

$$\chi_{DES}^2 = \sum_i \left( \frac{d_A(z_i, i)/r_s - d_A(z_i, \Omega_{m,0})/r_s}{\sigma_{d_A(z_i, i)/r_s}} \right)^2. \quad (\text{A.6})$$

The BAO data from Ly- $\alpha$  are of the form  $f_{BAO} = ((1+z) d_A/r_s, D_H/r_s)$  and are given by

$$\begin{array}{ccccc} z & (1+z) d_A/r_s & \sigma_{(1+z) d_A/r_s} & D_H/r_s & \sigma_{D_H/r_s} \\ 2.35 & 36.3 & 1.8 & 9.2 & 0.36 \end{array} \quad (\text{A.7})$$

with the  $\chi^2$  being

$$\chi_{Ly-\alpha}^2 = \sum_i \left( \frac{f_{BAO,i} - f_{BAO}(z_i, \Omega_{m,0})}{\sigma_{f_{BAO}}} \right)^2. \quad (\text{A.8})$$

The DR14 LRG and quasar BAO data assume  $r_{s, fid} = 147.78$  and are given by  $D_V/r_s = 1/d_z$

$$\begin{array}{ccc} z & 1/d_z & \sigma_{1/d_z} \\ 0.72 & 2353/r_{s, fid} & 62/r_{s, fid} \\ 1.52 & 3843/r_{s, fid} & 147/r_{s, fid} \end{array} \quad (\text{A.9})$$

and the  $\chi^2$  being

$$\chi_{LRG,Q}^2 = \sum_i \left( \frac{1/d_{z,i} - 1/d_z(z_i, \Omega_{m,0})}{\sigma_{1/d_{z,i}}} \right)^2. \quad (\text{A.10})$$

Finally, the total  $\chi^2$  is

$$\chi_{tot}^2 = \chi_{6dFGS,Wig}^2 + \chi_{MGS,SDSS}^2 + \chi_{DES}^2 + \chi_{Ly-\alpha}^2 + \chi_{LRG,Q}^2. \quad (\text{A.11})$$

## References

- Abbott, T. M. C., Abdalla, F. B., Alarcon, A., et al. 2019, MNRAS, 483, 4866  
Aguirre, A. & Haiman, Z. 2000, ApJ, 532, 28  
Aguirre, A. N. 1999, ApJ, 525, 583  
Ahlers, M. 2009, PRD, 80, 023513  
Akrami, Y., Scott, P., Edsjo, J., Conrad, J., & Bergstrom, L. 2010, JHEP, 04, 057  
Albrecht, A., Bernstein, G., Cahn, R., et al. 2006, arXiv e-prints, arXiv:astro-ph/0609591  
Amendola, L., Appleby, S., Avgoustidis, A., et al. 2018, Living Rev. Rel., 21, 2  
Anderson, L., Aubourg, É., Bailey, S., et al. 2014, MNRAS, 441, 24  
Arjona, R. 2020, arXiv:2002.12700  
Arjona, R. & Nesseris, S. 2019, arXiv e-prints, arXiv:1910.01529  
Arjona, R. & Nesseris, S. 2020, arXiv e-prints, arXiv:2001.11420  
Astier, P., Balland, C., Brescia, M., et al. 2014, A&A, 572, A80  
Ata, M., Baumgarten, F., Bautista, J., et al. 2018, MNRAS, 473, 4773  
Avgoustidis, A., Burrage, C., Redondo, J., Verde, L., & Jimenez, R. 2010, JCAP, 10, 024  
Avgoustidis, A., Génova-Santos, R. T., Luzzi, G., & Martins, C. J. A. P. 2016, PRD, 93, 043521  
Avgoustidis, A., Luzzi, G., Martins, C. J. A. P., & Monteiro, A. M. R. V. L. 2012, JCAP, 02, 013

- Avgoustidis, A., Martins, C. J. A. P., Monteiro, A. M. R. V. L., Vielzeuf, P. E., & Luzzi, G. 2014, JCAP, 06, 062
- Avgoustidis, A., Verde, L., & Jimenez, R. 2009, JCAP, 06, 012
- Bassett, B. A. & Kunz, M. 2004, PRD, 69, 101305
- Batell, B. & Gherghetta, T. 2006, PRD, 73, 045016
- Bautista, J. E., Vargas-Magaña, M., Dawson, K. S., et al. 2018, ApJ, 863, 110
- Beutler, F., Blake, C., Colless, M., et al. 2011, MNRAS, 416, 3017
- Blake, C., Brough, S., Colless, M., et al. 2012, MNRAS, 425, 405
- Blomqvist, M., du Mas des Bourboux, H., Busca, N. G., et al. 2019, A&A, 629, A86
- Bogdanos, C. & Nesseris, S. 2009, JCAP, 05, 006
- Brax, P., Burrage, C., Davis, A.-C., Seery, D., & Weltman, A. 2010, PRD, 81, 103524
- Burrage, C. 2008, PRD, 77, 043009
- Conley, A., Guy, J., Sullivan, M., et al. 2011, ApJS, 192, 1
- Corasaniti, P. S. 2006, MNRAS, 372, 191
- Costille, A., Caillat, A., Rossin, C., et al. 2018, in Space Telescopes and Instrumentation 2018: Optical, Infrared, and Millimeter Wave, ed. M. Lystrup, H. A. MacEwen, G. G. Fazio, N. Batalha, N. Siegler, & E. C. Tong, Vol. 10698, International Society for Optics and Photonics (SPIE), 730 – 744
- Cropper, M., Pottinger, S., Azzollini, R., et al. 2018, in Space Telescopes and Instrumentation 2018: Optical, Infrared, and Millimeter Wave, ed. M. Lystrup, H. A. MacEwen, G. G. Fazio, N. Batalha, N. Siegler, & E. C. Tong, Vol. 10698, International Society for Optics and Photonics (SPIE), 709 – 729
- Csáki, C., Kaloper, N., & Terning, J. 2002, PRL, 88, 161302
- Cuesta, A. J., Verde, L., Riess, A., & Jimenez, R. 2015, MNRAS, 448, 3463
- DESI Collaboration: Aghamousa, A., Aguilar, J., Ahlen, S., et al. 2016, arXiv e-prints, arXiv:1611.00036
- Eisenstein, D. J. & Hu, W. 1998, ApJ, 496, 605
- Etherington, I. M. H. 1933, Philos. Mag., 15, 761
- Euclid Collaboration: Blanchard, A., Camera, S., Carbone, C., et al. 2019, arXiv e-prints, arXiv:1910.09273
- Font-Ribera, A., McDonald, P., Mostek, N., et al. 2014, JCAP, 05, 023
- Gil-Marín, H., Percival, W. J., Cuesta, A. J., et al. 2016, MNRAS, 460, 4210
- Gong, Y., Cooray, A., & Chen, X. 2010, ApJ, 709, 1420
- Hogg, N. B., Martinelli, M., & Nesseris, S. 2020, arXiv:2007.14335
- Holanda, R., Gonçalves, R., & Alcaniz, J. 2012, JCAP, 06, 022
- Holanda, R., Lima, J., & Ribeiro, M. 2010, ApJ Lett., 722, L233
- Holdom, B. 1986, Phys. Lett. B, 166, 196
- Jaeckel, J. & Ringwald, A. 2010, Ann. Rev. Nucl. Part. Sci., 60, 405
- Kowalski, M., Rubin, D., Aldering, G., et al. 2008, ApJ, 686, 749
- Laureijs, R., Amiaux, J., Arduini, S., et al. 2011, arXiv e-prints, arXiv:1110.3193
- Leite, A. C. O., Martins, C. J. A. P., Molaro, P., Corre, D., & Cristiani, S. 2016, PRD, 94, 123512
- Liao, K. 2019, ApJ, 885, 70
- Liao, K., Li, Z., Cao, S., et al. 2016, ApJ, 822, 74
- Lima, J. A. S., Silva, A. I., & Viegas, S. M. 2000, MNRAS, 312, 747
- Liske, J. et al. 2014, Top Level Requirements For ELT-HIRES, Document ESO 204697 Version 1
- LSST Science Collaboration: Abell, P. A., Allison, J., Anderson, S. F., et al. 2009, arXiv e-prints, arXiv:0912.0201
- Luzzi, G., Shimon, M., Lamagna, L., et al. 2009, ApJ, 705, 1122
- Ma, C. & Corasaniti, P.-S. 2018, ApJ, 861, 124
- Maartens, R. 2011, Phil. Trans. Roy. Soc. Lond. A, 369, 5115
- Ménard, B., Nestor, D., Turnshek, D., et al. 2008, MNRAS, 385, 1053
- More, S., Bovy, J., & Hogg, D. W. 2009, ApJ, 696, 1727
- Mörtsell, E., Bergström, L., & Goobar, A. 2002, PRD, 66, 047702
- Nesseris, S. & García-Bellido, J. 2012, JCAP, 11, 033
- Nesseris, S. & García-Bellido, J. 2013, PRD, 88, 063521
- Nesseris, S. & Shafieloo, A. 2010, MNRAS, 408, 1879
- Noterdaeme, P., Petitjean, P., Srianand, R., Ledoux, C., & López, S. 2011, A&A, 526, L7
- Ntelis, P. et al. 2017, JCAP, 06, 019
- Pepe, F., Cristiani, S., Rebolo, R., et al. 2013, The Messenger, 153, 6
- Planck Collaboration: Aghanim, N., Akrami, Y., Ashdown, M., et al. 2018, arXiv e-prints, arXiv:1807.06209
- Pozzetti, L., Hirata, C. M., Geach, J. E., et al. 2016, A&A, 590, A3
- Ross, A. J., Samushia, L., Howlett, C., et al. 2015, MNRAS, 449, 835
- Sapone, D., Majerotto, E., & Nesseris, S. 2014, PRD, 90, 023012
- Scolnic, D. M., Jones, D. O., Rest, A., et al. 2018, ApJ, 859, 101
- Stern, D., Jimenez, R., Verde, L., Kamionkowski, M., & Stanford, S. 2010, JCAP, 02, 008
- Svrcek, P. & Witten, E. 2006, JHEP, 06, 051
- Torrado, J. & Lewis, A. 2020, arXiv e-prints, arXiv:2005.05290
- Wang, Y., Chuang, C.-H., & Hirata, C. M. 2013, MNRAS, 430, 2446
- Webb, J. K., King, J. A., Murphy, M. T., et al. 2011, PRL, 107, 191101
- Xu, X., Padmanabhan, N., Eisenstein, D. J., Mehta, K. T., & Cuesta, A. J. 2012, MNRAS, 427, 2146
- Yang, T., Holanda, R., & Hu, B. 2019, Astropart. Phys., 108, 57
- <sup>1</sup> Instituto de Física Teórica UAM-CSIC, Campus de Cantoblanco, E-28049 Madrid, Spain
- <sup>2</sup> Centro de Astrofísica da Universidade do Porto, Rua das Estrelas, 4150-762 Porto, Portugal
- <sup>3</sup> Instituto de Astrofísica e Ciências do Espaço, Universidade do Porto, CAUP, Rua das Estrelas, PT4150-762 Porto, Portugal
- <sup>4</sup> Departamento de Física, FCFM, Universidad de Chile, Blanco Encalada 2008, Santiago, Chile
- <sup>5</sup> Institute of Space Sciences (ICE, CSIC), Campus UAB, Carrer de Can Magrans, s/n, 08193 Barcelona, Spain
- <sup>6</sup> Institut d'Estudis Espacials de Catalunya (IEEC), 08034 Barcelona, Spain
- <sup>7</sup> School of Physics and Astronomy, University of Nottingham, University Park, Nottingham NG7 2RD, UK
- <sup>8</sup> INFN-Sezione di Torino, Via P. Giuria 1, I-10125 Torino, Italy
- <sup>9</sup> Dipartimento di Fisica, Università degli Studi di Torino, Via P. Giuria 1, I-10125 Torino, Italy
- <sup>10</sup> INAF-Osservatorio Astrofisico di Torino, Via Osservatorio 20, I-10025 Pino Torinese (TO), Italy
- <sup>11</sup> INAF-IASF Milano, Via Alfonso Corti 12, I-20133 Milano, Italy
- <sup>12</sup> AIM, CEA, CNRS, Université Paris-Saclay, Université Paris Diderot, Sorbonne Paris Cité, F-91191 Gif-sur-Yvette, France
- <sup>13</sup> Université PSL, Observatoire de Paris, Sorbonne Université, CNRS, LERMA, F-75014, Paris, France
- <sup>14</sup> CEICO, Institute of Physics of the Czech Academy of Sciences, Na Slovance 2, Praha 8, Czech Republic
- <sup>15</sup> Institut de Recherche en Astrophysique et Planétologie (IRAP), Université de Toulouse, CNRS, UPS, CNES, 14 Av. Edouard Belin, F-31400 Toulouse, France
- <sup>16</sup> Université St Joseph; UR EGFEM, Faculty of Sciences, Beirut, Lebanon
- <sup>17</sup> Astrophysics Research Institute, Liverpool John Moores University, 146 Brownlow Hill, Liverpool L3 5RF, UK
- <sup>18</sup> INAF-Osservatorio di Astrofisica e Scienza dello Spazio di Bologna, Via Piero Gobetti 93/3, I-40129 Bologna, Italy
- <sup>19</sup> INAF-Osservatorio Astronomico di Padova, Via dell'Osservatorio 5, I-35122 Padova, Italy
- <sup>20</sup> Max Planck Institute for Extraterrestrial Physics, Giessenbachstr. 1, D-85748 Garching, Germany
- <sup>21</sup> INFN-Sezione di Roma Tre, Via della Vasca Navale 84, I-00146, Roma, Italy
- <sup>22</sup> Department of Mathematics and Physics, Roma Tre University, Via della Vasca Navale 84, I-00146 Rome, Italy
- <sup>23</sup> INAF-Osservatorio Astronomico di Roma, Via Frascati 33, I-00078 Monteporzio Catone, Italy
- <sup>24</sup> INAF-Osservatorio Astronomico di Capodimonte, Via Moirariello 16, I-80131 Napoli, Italy
- <sup>25</sup> Institut de Física d'Altes Energies IFAE, 08193 Bellaterra, Barcelona, Spain
- <sup>26</sup> Department of Physics "E. Pancini", University Federico II, Via Cinthia 6, I-80126, Napoli, Italy
- <sup>27</sup> INFN section of Naples, Via Cinthia 6, I-80126, Napoli, Italy
- <sup>28</sup> Centre National d'Etudes Spatiales, Toulouse, France
- <sup>29</sup> Institute for Astronomy, University of Edinburgh, Royal Observatory, Blackford Hill, Edinburgh EH9 3HJ, UK
- <sup>30</sup> European Space Agency/ESRIN, Largo Galileo Galilei 1, 00044 Frascati, Roma, Italy
- <sup>31</sup> ESAC/ESA, Camino Bajo del Castillo, s/n., Urb. Villafranca del Castillo, 28692 Villanueva de la Cañada, Madrid, Spain
- <sup>32</sup> Department of Astronomy, University of Geneva, ch. d'Écogia 16, CH-1290 Versoix, Switzerland
- <sup>33</sup> Univ Lyon, Univ Claude Bernard Lyon 1, CNRS/IN2P3, IP2I Lyon, UMR 5822, F-69622, Villeurbanne, France
- <sup>34</sup> INAF-Osservatorio Astronomico di Trieste, Via G. B. Tiepolo 11, I-34131 Trieste, Italy
- <sup>35</sup> Istituto Nazionale di Astrofisica (INAF) - Osservatorio di Astrofisica e Scienza dello Spazio (OAS), Via Gobetti 93/3, I-40127 Bologna, Italy
- <sup>36</sup> Dipartimento di Fisica e Astronomia, Università di Bologna, Via Gobetti 93/2, I-40129 Bologna, Italy

- <sup>37</sup> Istituto Nazionale di Fisica Nucleare, Sezione di Bologna, Via Irnerio 46, I-40126 Bologna, Italy
- <sup>38</sup> Universitäts-Sternwarte München, Fakultät für Physik, Ludwig-Maximilians-Universität München, Scheinerstrasse 1, 81679 München, Germany
- <sup>39</sup> Institute of Theoretical Astrophysics, University of Oslo, P.O. Box 1029 Blindern, N-0315 Oslo, Norway
- <sup>40</sup> Jet Propulsion Laboratory, California Institute of Technology, 4800 Oak Grove Drive, Pasadena, CA, 91109, USA
- <sup>41</sup> von Hoerner & Sulger GmbH, Schloßplatz 8, D-68723 Schwetzingen, Germany
- <sup>42</sup> Max-Planck-Institut für Astronomie, Königstuhl 17, D-69117 Heidelberg, Germany
- <sup>43</sup> Aix-Marseille Univ, CNRS/IN2P3, CPPM, Marseille, France
- <sup>44</sup> Mullard Space Science Laboratory, University College London, Holmbury St Mary, Dorking, Surrey RH5 6NT, UK
- <sup>45</sup> University of Lyon, UCB Lyon 1, CNRS/IN2P3, IUF, IP2I Lyon, France
- <sup>46</sup> Université de Genève, Département de Physique Théorique and Centre for Astroparticle Physics, 24 quai Ernest-Ansermet, CH-1211 Genève 4, Switzerland
- <sup>47</sup> Department of Physics and Helsinki Institute of Physics, Gustaf Hållströmin katu 2, 00014 University of Helsinki, Finland
- <sup>48</sup> NOVA optical infrared instrumentation group at ASTRON, Oude Hoogeveensedijk 4, 7991PD, Dwingeloo, The Netherlands
- <sup>49</sup> Argelander-Institut für Astronomie, Universität Bonn, Auf dem Hügel 71, 53121 Bonn, Germany
- <sup>50</sup> Institute for Computational Cosmology, Department of Physics, Durham University, South Road, Durham, DH1 3LE, UK
- <sup>51</sup> Université de Paris, F-75013, Paris, France, LERMA, Observatoire de Paris, PSL Research University, CNRS, Sorbonne Université, F-75014 Paris, France
- <sup>52</sup> Observatoire de Sauverny, Ecole Polytechnique Fédérale de Lausanne, CH-1290 Versoix, Switzerland
- <sup>53</sup> INFN-Sezione di Bologna, Viale Berti Pichat 6/2, I-40127 Bologna, Italy
- <sup>54</sup> Institut de Física d'Altes Energies (IFAE), The Barcelona Institute of Science and Technology, Campus UAB, 08193 Bellaterra (Barcelona), Spain
- <sup>55</sup> Space Science Data Center, Italian Space Agency, via del Politecnico snc, 00133 Roma, Italy
- <sup>56</sup> Institute of Space Science, Bucharest, Ro-077125, Romania
- <sup>57</sup> INFN-Padova, Via Marzolo 8, I-35131 Padova, Italy
- <sup>58</sup> Dipartimento di Fisica e Astronomia "G.Galilei", Università di Padova, Via Marzolo 8, I-35131 Padova, Italy
- <sup>59</sup> Instituto de Astrofísica e Ciências do Espaço, Faculdade de Ciências, Universidade de Lisboa, Tapada da Ajuda, PT-1349-018 Lisboa, Portugal
- <sup>60</sup> Departamento de Física, Faculdade de Ciências, Universidade de Lisboa, Edifício C8, Campo Grande, PT1749-016 Lisboa, Portugal
- <sup>61</sup> Universidad Politécnica de Cartagena, Departamento de Electrónica y Tecnología de Computadoras, 30202 Cartagena, Spain
- <sup>62</sup> Infrared Processing and Analysis Center, California Institute of Technology, Pasadena, CA 91125, USA